Melt network reorientation and crystallographic preferred orientation development in sheared partially molten rocks

C. Seltzer[1], M. Peč[1], M.E. Zimmerman[2], D.L. Kohlstedt[2]

[1]Department of Earth, Atmospheric and Planetary Sciences, Massachusetts Institute of Technology, Cambridge, MA-02139

[2]Department of Earth and Environmental Sciences, University of Minnesota, Minneapolis, MN-55455

Corresponding author: Cassandra Seltzer (cseltz@mit.edu)

Key Points

1. The melt network in a deforming partially molten rock responds more quickly to a changing stress field than do its crystalline axes.
2. Grain-scale melt preferred orientation forms parallel to the maximum principal stress at the onset of deformation.
3. Rapid changes to seismic anisotropy observed in a deforming partially molten rock can be attributed to reorientation of melt.

Abstract:

As partially molten rocks deform, they develop melt preferred orientations, shape preferred orientations, and crystallographic preferred orientations (MPOs, SPOs and CPOs). We investigated the co-evolution of these preferred orientations in experimentally deformed partially molten rocks, then calculated the influence of MPO and CPO on seismic anisotropy. Olivine-basalt aggregates containing 2 to 4 wt% melt were deformed in general shear at a temperature of 1250°C under a confining pressure of 300 MPa at shear stresses of $\tau = 0$ to 175 MPa to shear strains of $\gamma = 0$ to 2.3. Grain-scale melt pockets developed a MPO parallel to the maximum principal stress, σ_1, at $\gamma < 0.4$. At higher strains, the grain-scale MPO remained parallel to σ_1, but incipient, sample-scale melt bands formed at ~20° to σ_1. An initial SPO and CPO were induced during sample preparation, with [100] and [001] axes girdled perpendicular to the long axis of the sample. At the highest explored strain, a strong SPO was established, and the [100] axes of the CPO clustered nearly parallel to the shear plane. Our results demonstrate that grain-scale and sample-scale alignments of melt pockets are distinct. Furthermore, the melt and the solid microstructures evolve on different timescales: in planetary bodies, changes in the stress field will first drive a relatively rapid reorientation of the melt network, followed by a relatively slow realignment of the crystallographic axes. Rapid changes to seismic anisotropy in a deforming partially molten aggregate are thus caused by MPO rather than CPO.

Plain language summary:

We studied the influence of melt alignment and crystal alignment on the properties of partially melted regions in planetary bodies. Molten and crystalline elements within the rocks in these layers can deform and reorient in response to stress, but it is difficult to predict exactly how the realignment of each phase affects seismic properties of the rocks. Reorientation of melt networks during deformation of partially molten rocks is not well constrained, as experiments and computational models disagree on the most favorable alignment of melt pockets. Here, we measured the angles and shapes of melt and crystals in experimentally deformed partially molten

rocks, then calculated seismic properties of the deformed rocks. We found that melt pockets change orientation and shape quickly, but crystals take longer to reorient. This indicates that immediate changes to seismic properties after a sudden change in stress field are caused by melt, rather than by crystals. We also discovered that experimental observations and modeling predictions of melt orientations do agree, but only at small scales. Our results show that when stress fields abruptly change in Earth and other planetary bodies, melt pocket orientations will control seismic properties and are the best instantaneous indicators of these stress changes.

1. Introduction

Partial melting often occurs alongside sites of rapid deformation in Earth's lithosphere. In response to deformation, the molten and crystalline components of partially molten rocks align, leading to anisotropies in mechanical, transport, and seismic properties (Blackman & Kendall, 1997; Daines & Kohlstedt, 1997; Holtzman et al., 2003; Holtzman & Kendall, 2010; Long & Becker, 2010; Savage, 1999; Taylor-West & Katz, 2015). The interpretation of seismic images obtained from deforming partially molten regions of Earth is, however, not straightforward. Seismic waves propagating through partially molten rocks are sensitive to the bulk and shear moduli, which are determined by the poroelastic properties of the skeletal network of solid grains and the viscous properties and geometry of the interstitial melt phase (Holtzman & Kendall, 2010; Mainprice, 1997; Takei, 2001). As molten and solid rock components have distinct seismic properties, the orientations of both phases contribute to the seismic anisotropy observed in Earth's upper mantle and crust (Almqvist & Mainprice, 2017; Hansen et al., 2021).

Experiments provide an important benchmark for melt and crystallographic preferred orientations in deformed partially molten mantle rocks. However, experimental results and modeling assumptions often disagree on the orientation of the melt network. Previous experimental studies report an alignment of the long axes of melt pockets at 20° to the direction of the maximum principal stress (Zimmerman et al., 1999) and, with increasing strain, the formation of melt-rich "bands" at a similar orientation (Holtzman et al., 2003; King et al., 2010). In contrast, some viscoelastic models and theories predict grain-scale melt alignment parallel to

the direction of the maximum principal stress, σ_1. (Hier-Majumder, 2011; Takei & Holtzman, 2009c; Taylor-West & Katz, 2015). To resolve differences between modeling and experimental results, we reexamined microstructures of deformed partially molten samples at both the grain scale and the sample scale.

The present study investigated the microstructural behavior of several deformed partially molten aggregates. The sample-scale behavior of one set of samples was previously reported in Zimmerman et al. (1999). In addition, the behavior of two additional samples deformed at higher stress conditions was examined. We characterize the co-evolution of melt preferred orientation (MPO) of the liquid network and crystallographic and shape preferred orientations (CPOs and SPOs) of the solid phase, from which we infer the influence of stress and strain on CPO, SPO and MPO development in the deformed samples. We then use our experimental results to calculate predicted seismic anisotropy in these samples, and discuss the relative importance of melt and crystalline orientations on seismic anisotropy in samples deformed to small strains.

2. Methods

2.1 Experimental deformation and imaging details

Samples of olivine ± orthopyroxene and 2-4 wt% mid-ocean ridge basalt (MORB) were created by hot pressing cold-pressed powders in a gas-medium deformation apparatus (Paterson, 1990) at 1250ºC at 300 MPa for ~3 hours. Samples were then cored and sliced from the hot-pressed cylinders and placed between thoriated tungsten pistons pre-cut at a 45º angle, as illustrated in Figure 1. These samples were subsequently deformed at the University of Minnesota in the gas-medium deformation apparatus at 1250ºC and 300 MPa confining pressure. Under strain rates of 10^{-4}-10^{-6} s^{-1}, samples reached shear stresses of τ = 50-175 MPa and strains of γ = 0.32-2.3. After deformation, samples were cut perpendicular to the shear plane and parallel to the shear direction, as indicated in Figure 2. A Zeiss Merlin scanning electron microscope (SEM) in the MIT Materials Research Laboratory was used to create backscattered electron (BSE) images at 15 – 20 kV accelerating voltage of these 2-D flat sections. In addition electron backscattered diffraction (EBSD) maps and energy dispersive spectra (EDS) maps were collected using a Camscan X500FE CrystalProbe at the Université Montpellier 2 at an acceleration voltage of 20 kV and a step size of 0.2 – 0.6 μm.

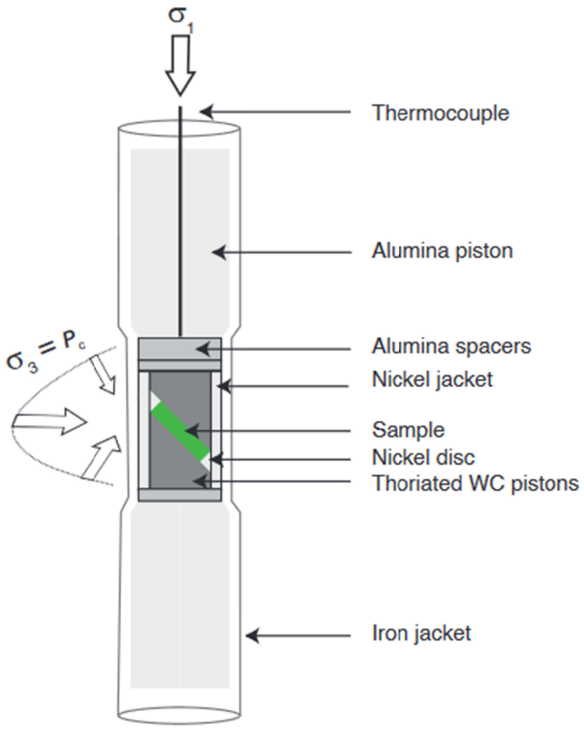

115

116 Figure 1: Schematic drawing of the sample setup for deformation experiments.

117

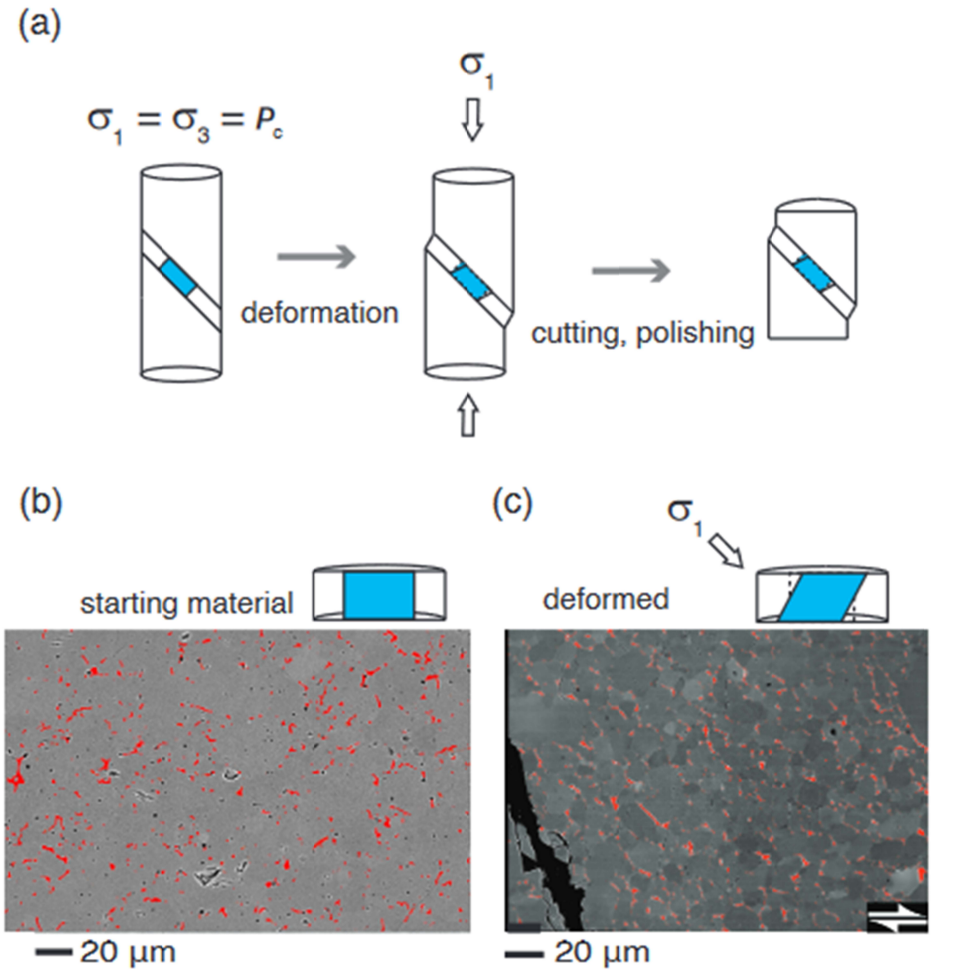

Figure 2: Sample preparation after deformation and orientation of cuts. (a) Experimental work flow for deformation and creation of 2-D sections. SEM images of orientation and appearance of the olivine-melt aggregates (b) prior to and (c) after deformation, with melt highlighted in red.

2.2 Quantitative image analysis methods

We used the projection-based method PAROR (Heilbronner and Barrett, 2014, Chapter 14) to analyze the grain-scale MPOs and SPOs. This method yields the direction of the longest and shortest projections of particle elements. In contrast to the more common ellipse-fitting method of determining short and long axes, PAROR does not require the shortest and longest directions to be perpendicular to each other and is therefore well suited for analyzing shapes of

130 irregular objects such as melt pockets. The shape preferred orientation, α_p, is calculated relative
131 to the shortest projection direction α_{min} such that
132
133 $$\alpha_p = 90^\circ - \alpha_{min} . \quad (1)$$
134
135 Note that values of α_p are symmetric around 180˚, so that for $\alpha_{min} > 90^\circ$, negative values
136 are converted to their positive conjugate (i.e., -30˚ is the same as 150˚). We described the
137 orientations of grains and melt pockets using an orientation distribution function (ODF)
138 visualized as rose diagrams, normalized such that the longest axis is 1 and the shortest axis is
139 reported as a percentage relative to the longest axis, as illustrated in Figure 3.
140 The strength of the preferred orientation is quantified by its bulk aspect ratio, *b*/*a*, a
141 comparison of the longest, *a*, and the shortest, *b*, projections of all the analyzed melt pockets. A
142 high value of the *b*/*a* ratio indicates that little difference exists between the shortest and longest
143 axes, and hence the shape is close to isotropic. In contrast, a lower value of *b*/*a* indicates a
144 stronger preferred orientation. We also calculated the size of segmented objects as an equivalent
145 area circle with diameter d_{equ}. Because both melt pocket size and grain size distributions
146 frequently follow a log-normal distribution, we report the mode of the log-normal probability
147 distribution as the most common size for melt pockets or grains in a given sample.
148 We analyzed the orientation of a sample-scale melt network with the autocorrelation
149 function (ACF; Heilbronner and Barrett, 2014, Chapter 20). The autocorrelation function
150 quantifies the orientation and spatial frequency of the patterns in an image without the
151 segmentation of individual features. This approach is therefore well suited for analyzing large-
152 scale, fine-feature patterns. Angles are measured counter-clockwise from 0° (east) to 180°
153 throughout this manuscript.
154

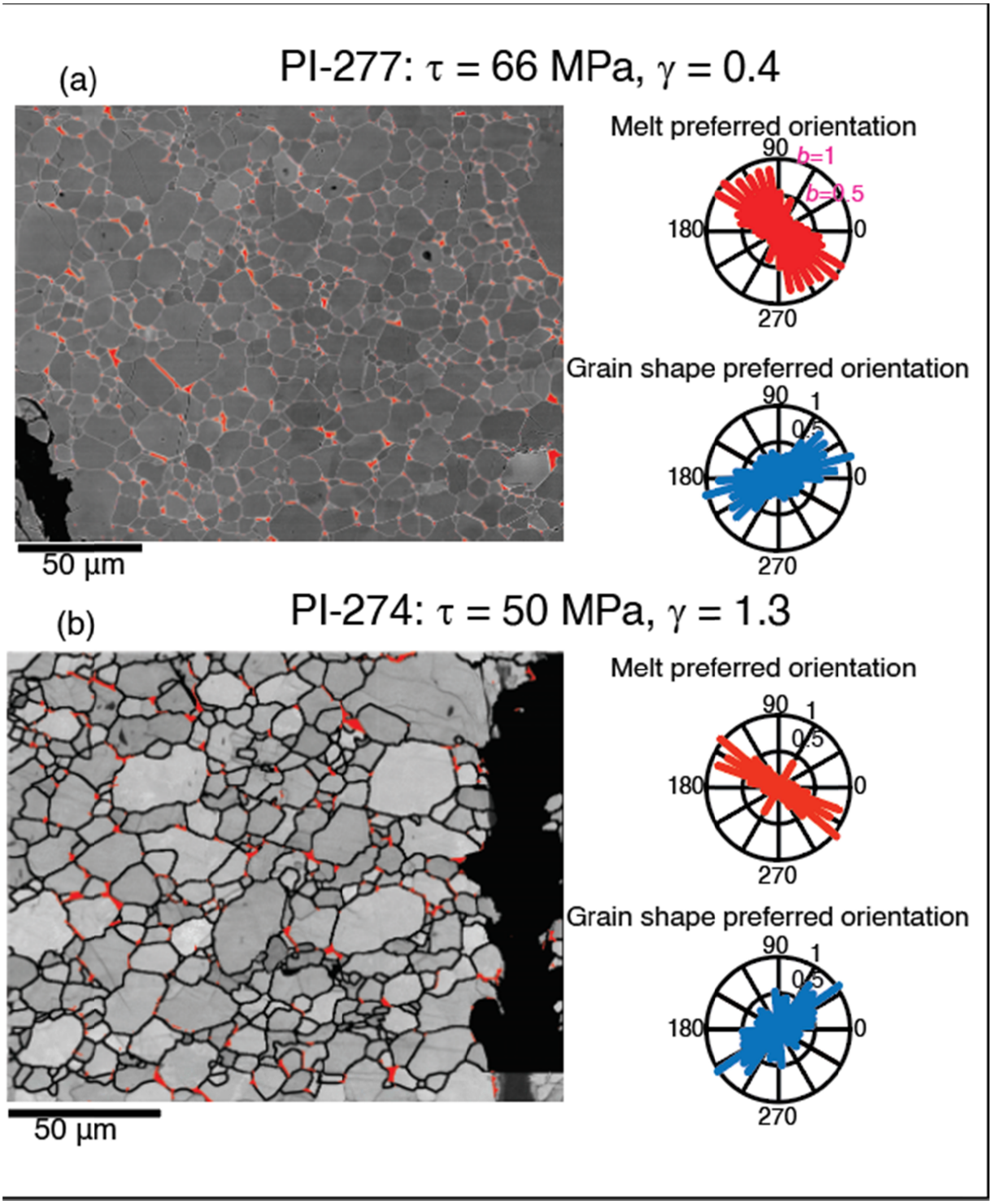

Figure 3: 2-D maps of two samples, one deformed to (a) low strain and the other to (b) high strain. The grains are outlined and melt pockets are highlighted in red overlaying SEM images of the samples. The melt and grain preferred orientations obtained from these images are represented as rose diagrams in red and blue, respectively.

2.3 Melt network image analysis

Melt pockets, which are 2-D cross-sections through a 3-D melt network, were analyzed at the grain scale and at the sample scale. To measure grain-scale MPO, individual pockets were traced from EDS and band-contrast images such as those in Figure 3, Figure 4a, and 4b. These traced images were then thresholded to binary, black and white images for segmentation. Only pockets above a minimum size of 10 pixels (at pixel resolutions of 0.02 – 0.4 μm) were analyzed so as to avoid effects from poorly defined small melt pockets. We quantified the MPO and strength of alignment in a sample based on two factors, orientation (α_p) and bulk aspect ratio (b/a), as described above.

To identify larger-scale melt patterns, we used EDS composition maps of calcium, an element not present in significant concentration in olivine, as a tracer for melt. We segmented these maps to create binary images of individual melt pockets, which we analyzed using the ACF over the entire sample imaged.

2.4 Grain-shape preferred orientation and crystallographic preferred orientation analyses

The shape preferred orientation was obtained from manual tracing of grains on SEM maps of the 2-D slices, as well as from EBSD data. We characterize the shape preferred orientation of the grains in the same manner as the grain-scale MPO described above. Representative data are displayed in Figure 3.

EBSD data were collected at two scales, analogous to the melt network analyses. A low-resolution map (0.6-μm step size) covered large parts of the whole sample, and a high-resolution map (0.2-μm step size) focused on the intracrystalline deformation features, highlighted in Figures 4c-d. The EBSD data were then analyzed using the MTEX toolbox (https://mtex-toolbox.github.io/) to characterize the 3-D orientation of the crystallographic axes. The crystallographic preferred orientation is defined by an ODF describing the direction of the three mutually perpendicular crystallographic axes in the olivine crystals in each sample. This ODF is represented graphically as a pole figure depicting multiples of uniform density (M.U.D.) in an equal-area, upper hemisphere projection, indicating areas of high and low concentrations of each of the three crystallographic axes of olivine, as indicated in Figures 4e-f. We also collected the misorientations of the subgrains in the high-resolution EBSD maps, defined by the difference in

191 internal pixel orientations from the mean orientation of an entire grain, which allowed us to
192 examine internal deformation of grains.
193
194 *2.5 Calculation of seismic anisotropy*
195 To constrain the microstructural contributions of MPO and CPO to the generation of
196 seismic anisotropy in olivine-melt aggregates, we followed the Gassman poroelastic differential
197 effective medium method as applied in a Matlab model, GassDEM (Kim et al., 2019). This
198 method uses the Voigt elastic tensor calculated from the CPO, then treats melt inclusions as an
199 oriented fluid-filled crack.
200 We modeled melt pockets as penny-shaped ellipsoids, in which the *a:b:c* axes of the
201 shape followed the ratio 1:*b*:1, where *b* is the shortest projection length of the melt pocket
202 normalized by the longest projection length (equivalent to the *b*/*a* reported for all MPOs), and
203 using the orientations of our MPOs such that the azimuth of an inclusion is the angle at which *b*
204 is oriented with 0˚ = E and 90˚ = N. These orientations were rotated during input into the
205 GassDEM interface, which takes 0˚ = N and 90˚ = W. We took the high-frequency elastic
206 constants of the resultant tensor calculated with 2.5 wt% melt.

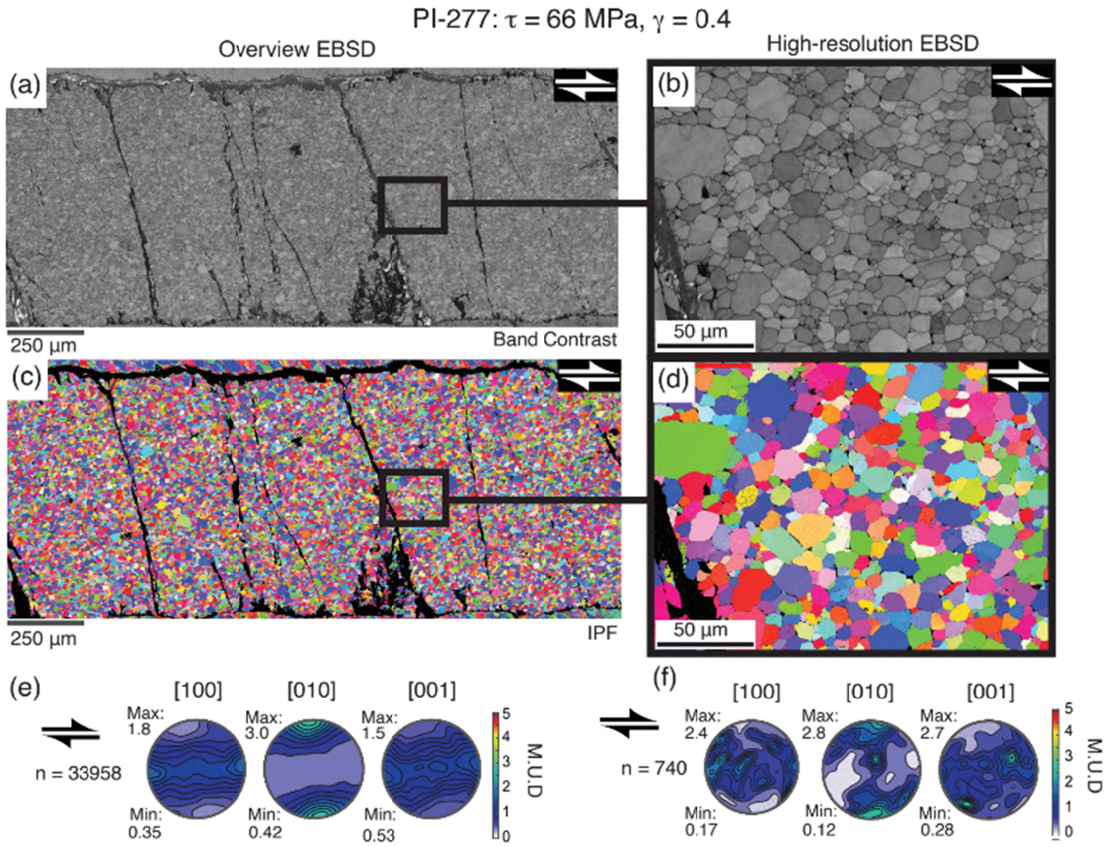

Figure 4: (a), (b) Band contrast images and (c), (d) orientation maps for sample PI-277. Pole figures are equal-area projections scaled as multiples of uniform distribution (M.U.D.). (e) Overview EBSD pole figures correspond to a larger number of crystals, while (f) high-resolution EBSD pole figures include a smaller number of crystals in greater detail, resulting in more pronounced point maxima.

3. Results

3.1 MPO - Melt preferred orientation

3.1.1 Grain-scale melt alignment

The individual orientations of grain-scale melt pockets, which were collected for all analyzed samples, are summarized in Figure 5. The melt preferred orientation in the starting material is very weak, and the *b*/*a* aspect ratio of 0.97 from all aggregated individual melt pockets indicates a nearly isotropic shape. The strength of the MPO increased at the onset of deformation and was fully established by $\gamma \approx 0.5$, with melt pockets oriented close to the direction of the maximum applied principal stress at 135˚. The MPO at this scale, once

established, was essentially independent of further strain; it varied by only ±5º from parallel to the loading direction, with one exception, over the entire range of strains and stresses explored.

The projection curves from the PAROR orientations in Figure 5b document that the strongest alignment, a *b*/*a* ratio of 0.72, formed by a strain of $\gamma = 0.4$. At strains of $\gamma > 0.4$, melt pockets also became slightly more isotropic with increasing strain. Melt pocket sizes also converged to a common size at low strains, as in Figure 5c. Starting material melt pocket size was ~2 µm, while melt pocket sizes shrank to ~0.9 µm by $\gamma = 0.4$ and converged to $d_{equ} \approx 0.5$ µm by $\gamma > 0.4$ regardless of the magnitude of stress or strain.

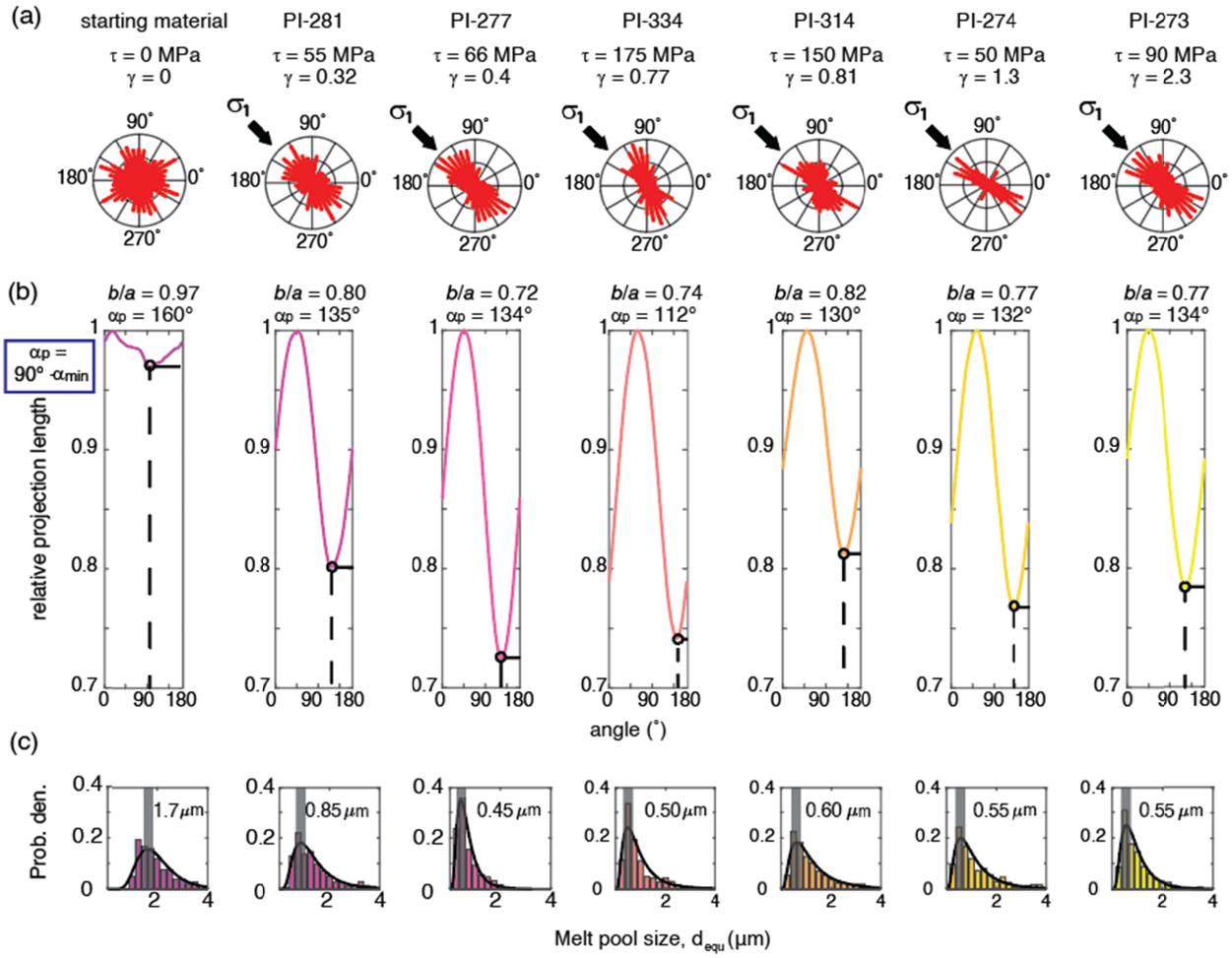

Figure 5: Evolution of MPO as a function of strain. (a) Rose diagrams from orientation of longest projection axes of each individual melt pocket, with the longest segments indicating the most common orientation of the longest projection axes. (b) Projection functions from SURFOR with minima (shortest projection axis) and the corresponding preferred orientation labeled. (c)

Melt pocket size histograms with log-normal fit overlain. The mode of the distribution is labeled and indicated with a gray bar.

3.1.2 Sample-scale melt alignment

The initial orientation and spatial distribution of melt at the sample scale was isotropic, as revealed by the ACF analyses of the binary images in Figure 7. At low strains, the spatial distribution of the melt remained isotropic, but the network of melt pockets developed a preferred orientation parallel to the direction of applied stress at the sample scale, in agreement with the orientation of melt observed at the grain scale. In the samples deformed to the highest strain, melt began to segregate into relatively melt-rich and melt-poor regions, and a secondary orientation at long correlation length scales (i.e., the spatial distance over which a feature can be correlated with itself) began to form at ~155˚ (~20˚ to σ_1, ~25˚ to the shear zone boundary). Short-correlation length scales (i.e., those close to the origin on the ACF plot) still retained an orientation sub-parallel to the loading direction.

3.1.3 Melt alignment summary

Rapid evolution of the MPO occurred in the earliest stages of shearing. A clear MPO parallel to σ_1 was already developed at a strain of $\gamma \approx 0.3$. The maximum strength of melt preferred orientation occurred at a strain of $\gamma \approx 0.4$. The MPO thus reached a steady state orientation and strength after only a relatively small strain increment, a trend that does not depend on stress within the studied range. The grain-scale MPO from smaller areas described in Section 3.1.1 has larger variations in orientation than ACF-derived orientations over much larger areas. At the highest strain explored, incipient segregation into melt-rich and melt-poor domains led to the development of a secondary preferred orientation at 25˚ to the shear zone boundary.

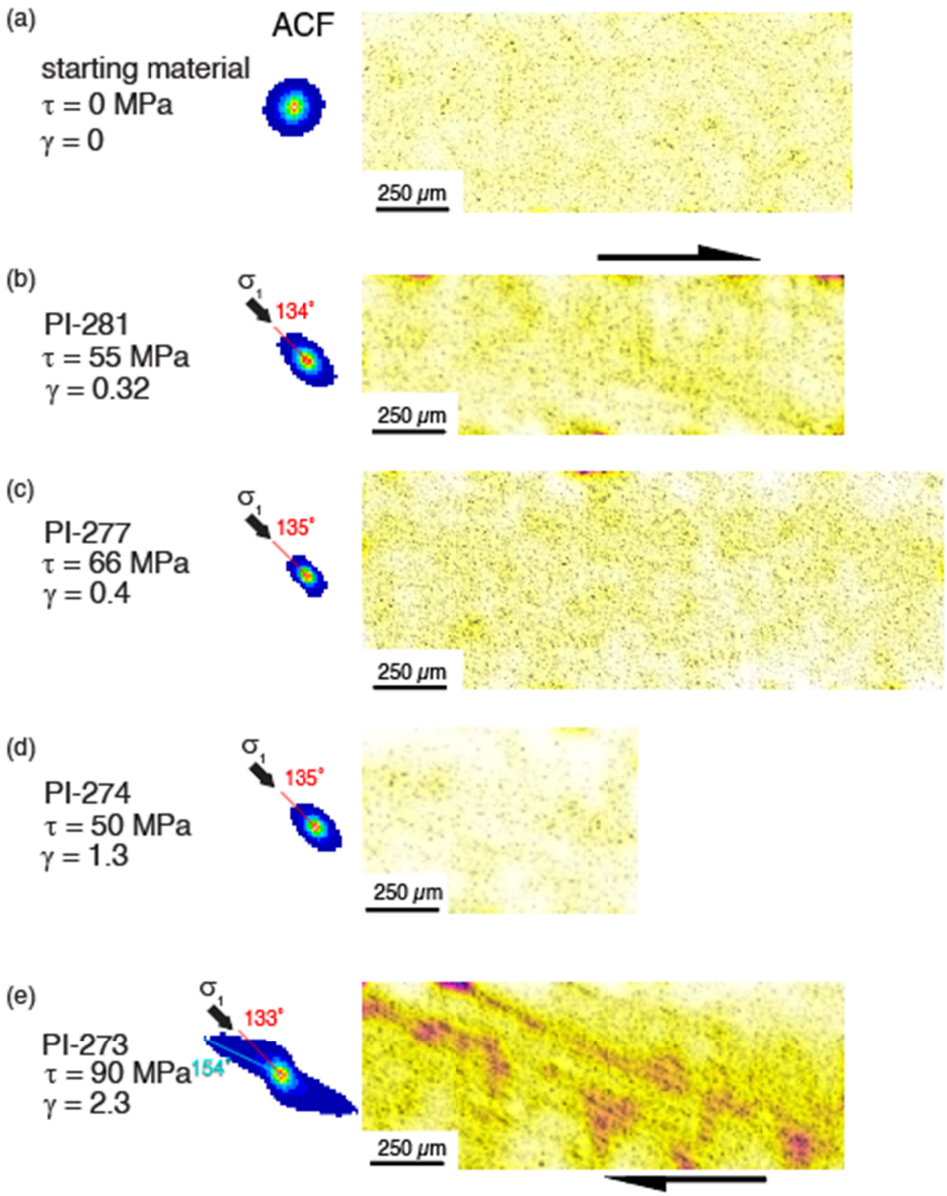

Figure 6: Sample-scale melt network analyzed by the autocorrelation function (ACF). Conditions of our (a) hot-pressed starting material and (b)-(e) four deformation experiments with each corresponding ACF (central column) and binary melt map contoured from low melt density, in white, to high melt density, in purple (rightmost column). The distance from the center of an ACF represents the length scale over which a feature can be correlated (i.e., closer to center of an ACF = shorter-scale feature correlation, while further away from the center of the ACF = longer-scale feature correlation).

3.2 Grain shape and crystallographic preferred orientation (SPO & CPO)

3.2.1 SPO - Shape preferred orientation

The SPO of all grains was analyzed, and is reported in Figure 7. At low strains, grains remained oriented approximately perpendicular to the direction of σ_1. This orientation did not evolve significantly with strain until $\gamma > 0.8$, at which point the orientation began to rotate into the instantaneous stretching direction, becoming closer to perpendicular to the direction of σ_1.

The bulk aspect ratios, *b*/*a*, and preferred orientations, α_p, of the grains (Figure 7b) did not change in a significant way as strain increases for $\gamma < 1.3$. The grain shape aspect ratios remained close to isotropic (with a minimum of 0.88 at $\gamma = 0$ and a maximum of 0.94 at $\gamma = 0.3$) for all but the sample deformed to the highest strain. A stronger SPO, indicated by a *b*/*a* of 0.79, formed by $\gamma = 1.3$, as long axes of the deforming grains began to align. This behavior indicates that the grain shape itself was changing slowly at lower strains but evolved into a stronger preferred orientation as strain increased to $0.8 > \gamma > 1.3$.

Grain sizes generally decreased with increasing stress. The distribution of grain sizes in the starting material (Figure 7c) peaked between 5 and 10 μm after hot-pressing for 3 h. At $\gamma = 0.3$, grains exhibited a normal distribution curve with a peak at ~9 μm, while all samples deformed to higher strain had a log-normal distribution curve of grain sizes peaking between 2 and 4 μm. Grain sizes, aspect ratios, and shape fabrics wavered around similar values at very low strains ($\gamma < 1.3$); at the highest strains examined here, both aspect ratios and grain sizes began to decrease. SPO thus required higher strains to develop and was less sensitive to the early stages of deformation than MPO.

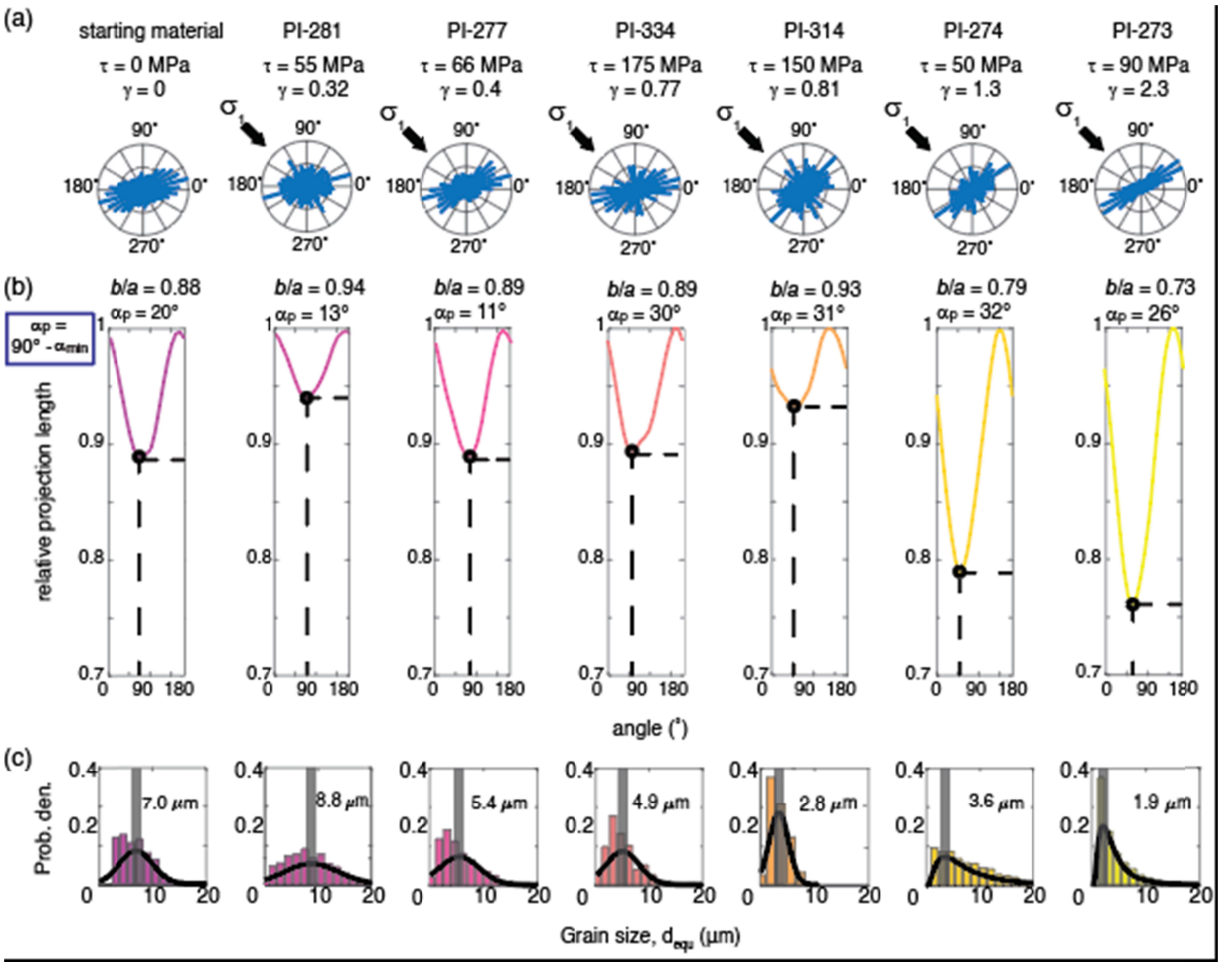

Figure 7: Grain SPO evolution as a function of strain. (a) Rose diagrams from orientation of longest projection axes of each individual grain. (b) Projection functions with minima (shortest projection axis) and the corresponding preferred orientation labeled. (c) Grain size distribution, with normal or log-normal fit overlain. The mode of the distribution is labeled and indicated with a gray bar.

3.2.2 CPO - Crystallographic preferred orientation

The CPOs of deformed samples in Figure 8 evolved with increasing strain. The starting material had a well-developed CPO with [010] axes aligned parallel to the long axis of the sample and the [100] and [001] axes in weak girdles perpendicular to the long axis of the sample. As strain increased, alignment of the [010] axes increased in strength, while the [100] and [001] axes remained girdled. At low strains, the orientations rotated antithetically away from the shear

plane, such that the [010] axes were 75-90° from the shear plane and the [100] and [001] axes girdled within 5° of the shear plane. At the highest strain reached in our experiments, $\gamma = 2.3$, the a-girdle rotated nearly parallel to σ_1 and developed stronger clustering, while the [001] axes began to cluster in the center of the pole figure. A secondary maximum orientation of the [100] axes developed 85-90° to σ_1.

The effect of increasing strain on intracrystalline structure is illustrated in Figure 9. As seen in Figure 9a, subgrains in olivine crystals increased in density and misorientation as strain increased; the starting material had a low subgrain density and low misorientation angles (<10°) within those subgrains, while the sample deformed to $\gamma = 2.3$ had subgrains with relatively high misorientations (>10°) in nearly every grain. Inverse pole figures of the misorientations demonstrate that, with increasing strain, rotation around the [001] axis became increasingly common. The development of a subordinate maximum also suggests rotation around the [010] axis.

Similar to SPOs, CPOs did not change much in the early stages of deformation. The orientations of the crystallographic axes shifted only slightly, as the [010] planes first rotated antithetically to the shearing direction and then rotated into the shear plane. At strains of $\gamma = 1.3$ - 2.3, the [010] planes were rotated slightly synthetical to the imposed shear direction. The strength of the CPO generally increased as strain increased.

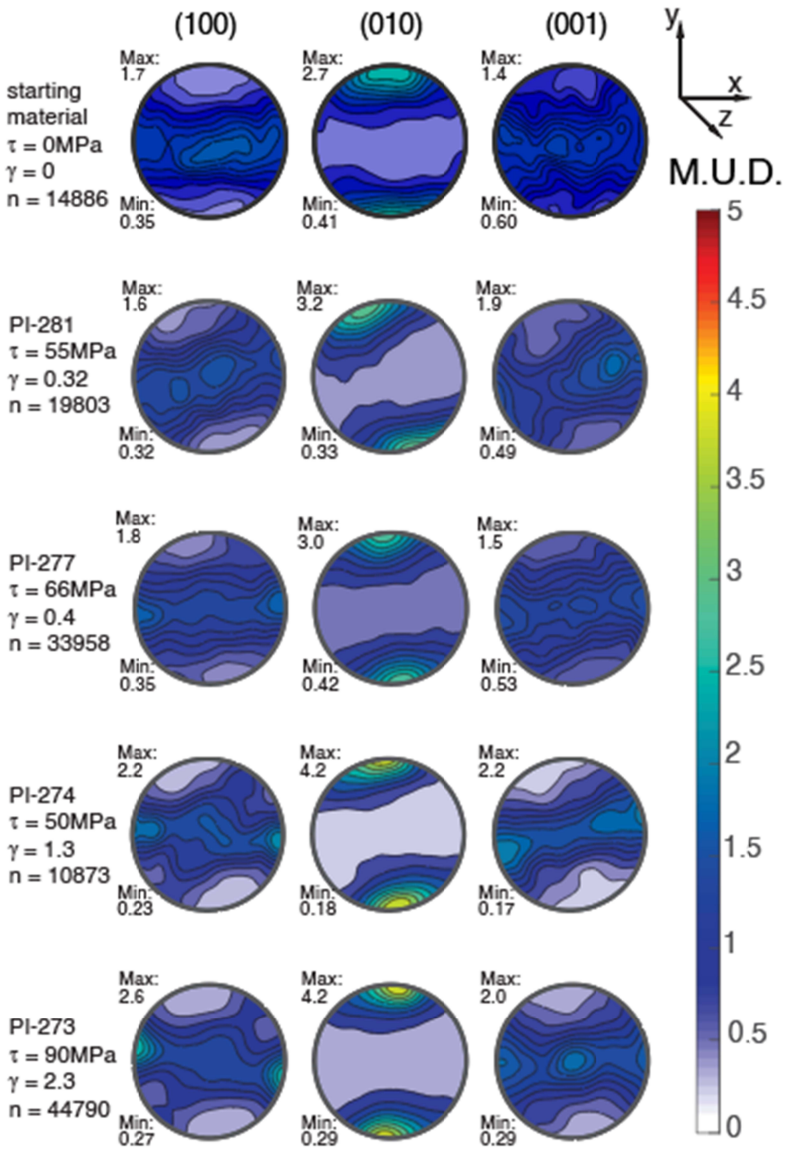

Figure 8: CPO evolution with increasing strain. Minima and maxima are reported as multiples of uniform distribution, M.U.D., and *n* is the number of grains surveyed in each map.

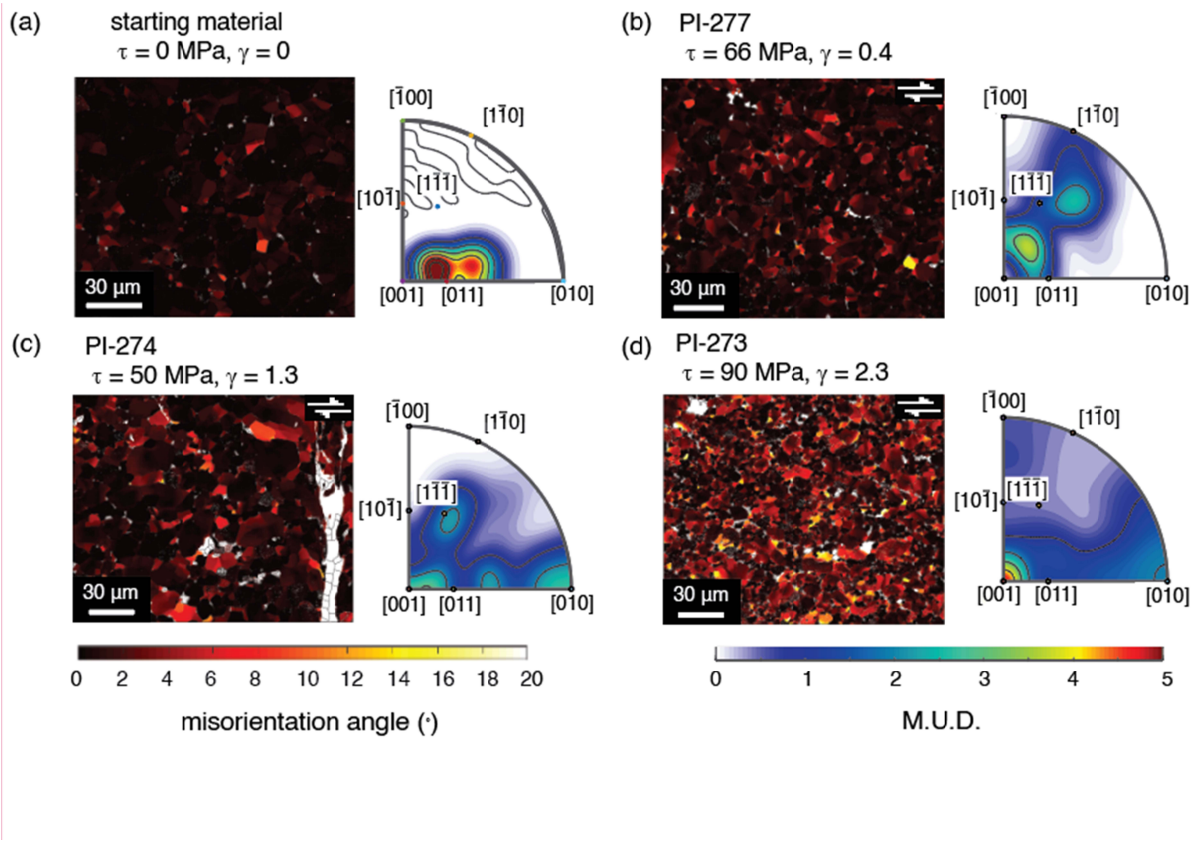

Figure 9: Misorientation maps and inverse pole figures of misorientation axes in crystallographic reference frame from (a) the starting material, (b) a sample sheared to low strain, and (c)-(d) two samples deformed to high strain. All images are shown at the same scale.

3.3 Calculation of seismic anisotropy

The effective calculated seismic anisotropy of each of our partially molten rocks is presented in Figure 10. We express three measures of seismic anisotropy: the % difference in Vp wavespeeds, calculated as the difference between fastest and slowest orientations within the tensor, the % difference in Vs wavespeeds, calculated as the greatest difference between Vs_1 and Vs_2 within the tensor, and the Vs_1 anisotropy, calculated as the greatest difference between Vs_1 wavespeeds. The pole figures in Figure 10 show the distribution of Vp wavespeeds, the distribution of the difference between Vs_1 and Vs_2 wavespeeds, and the velocity and polarization of Vs_1 waves.

At the onset of deformation, the calculated values of the seismic anisotropy decreased. However, at $\gamma \gtrsim 0.4$, the effective calculated values of seismic anisotropy increased with increasing strain. This behavior parallels the development of MPOs and CPOs with increasing strain. At low strains, the CPO was weak, and the MPO was oriented antithetical to the shearing direction and parallel to σ_1. The σ_1-parallel melt orientation was oblique to the orientation of the crystallographic axes, which were aligned in a girdle parallel to the shear plane. The anisotropy determined for our lower strain tests reflects a competition between MPO and CPO. As a result, the melt decreased the CPO-generated anisotropy with respect to a melt-free sample. As strain increased, the strength and direction of the preferred orientation of the melt network did not change, but the CPO became stronger and the [100] axes become more aligned parallel to the shear plane. At higher strains, the CPO developed a stronger alignment and became the dominant determinant of anisotropy. As this change occurred, the seismic anisotropy of Vp, Vs, and Vs_1 all steadily increased.

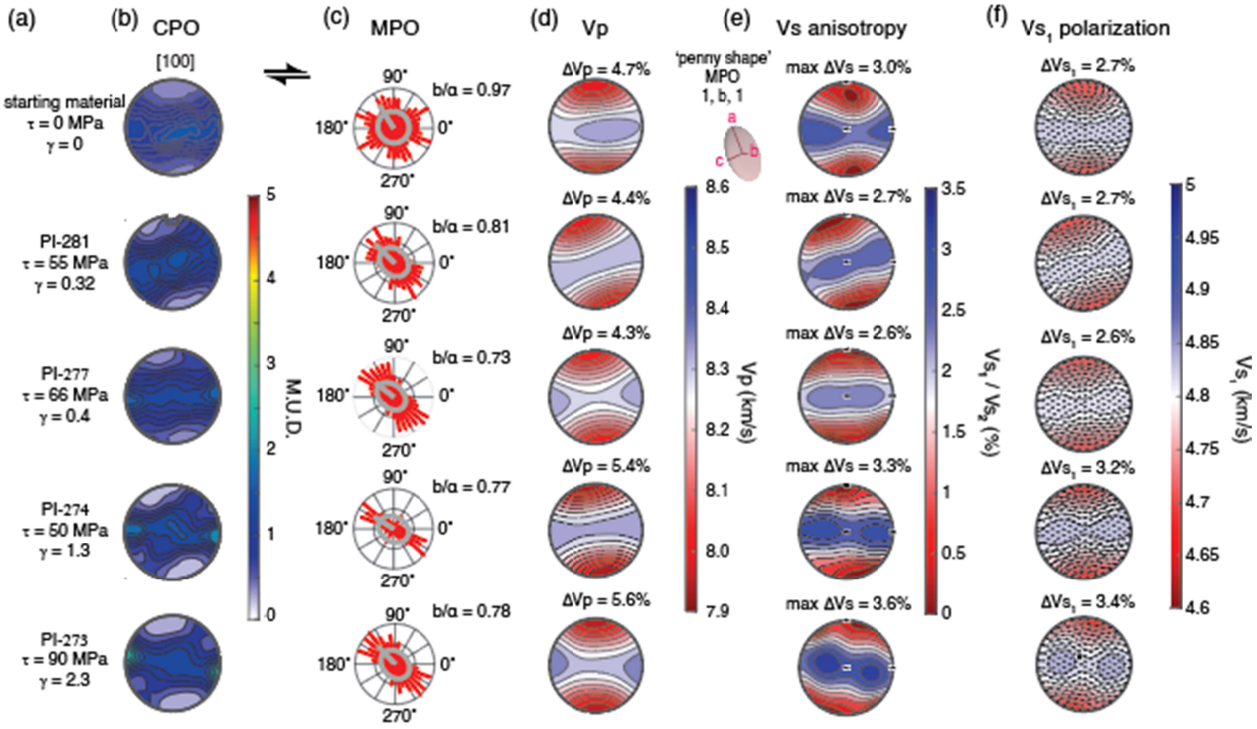

Figure 10. Calculated seismic anisotropy from our CPO and MPO data. (a) Individual experiment numbers and associated conditions, (b) a-axis orientation pole figures, and (c) MPO visualized in the rose diagrams. The mean melt inclusion shape and orientation is represented as a gray ellipsoid superimposed on rose diagrams for (d) Vp

anisotropy (difference between slowest and fastest p-wave velocity direction), (e) Vs anisotropy (difference between orthogonally polarized Vs_1 and Vs_2 velocities), and (f) Vs_1 polarization and velocity.

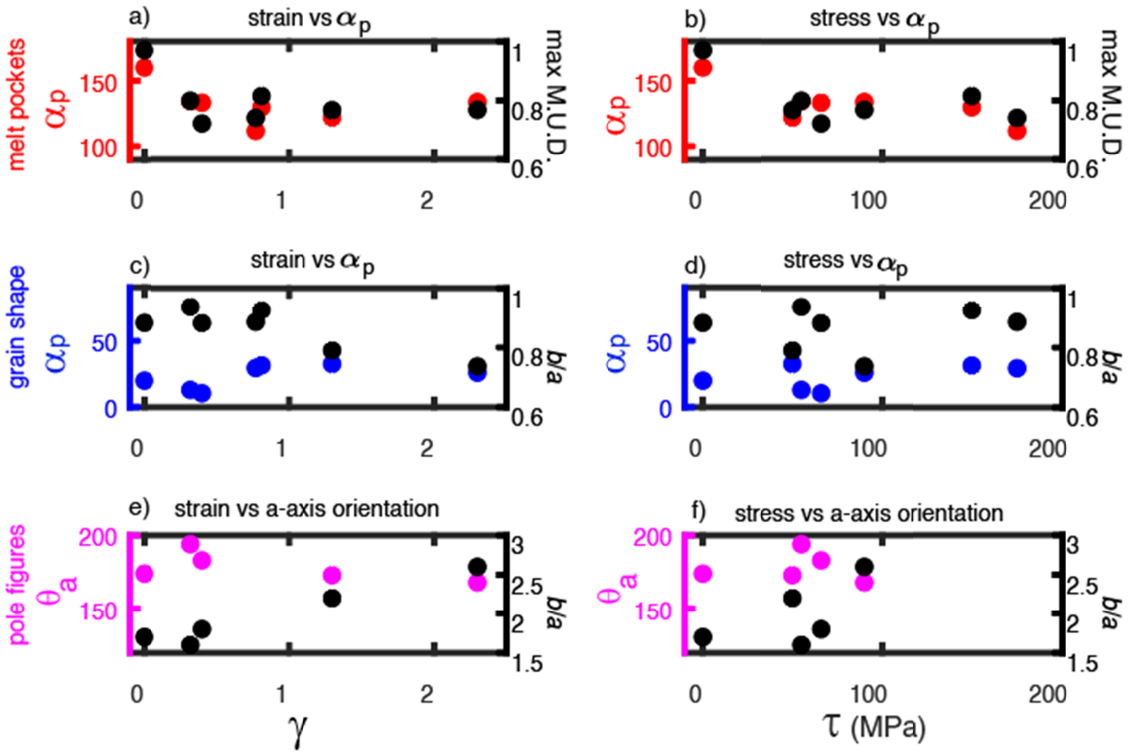

Figure 11. Summary of microstructural data. (a)-(d) Preferred orientation angle (from 0° = E) as a function of strain (a), (c) and stress (b), (d) for grain-scale melt pockets (a), (b) and grains (c), (d). Preferred orientation is reported as α_p, and the strength of the preferred orientation is indicated by the *b*/*a* aspect ratio of the fabric. (e)-(f) Orientation of the girdle formed by olivine [100] axes (θ_a) as a function of strain (e) and stress (f), with the strength of the preferred orientation reported as peak multiples of uniform distribution, such that a higher M.U.D. represents a higher concentration of axes aligned at this orientation. Note that CPO data are not available for the higher stress tests.

4. Discussion

4.1 MPO formation on grain scale and on sample scale

Our results demonstrate that MPOs evolve much more quickly at the onset of shear deformation than either SPO or CPO of the solid grains as summarized in Figure 11. The grain-scale MPO reacted to changing conditions nearly instantaneously, and a MPO different than that of the starting material formed at the onset of deformation ($0 < \gamma < 0.32$). A peak in MPO strength was reached at a shear strain of 0.4, after which the MPO oscillated around a steady state value; the orientation remained approximately parallel to the direction of maximum principal stress, and melt pool sizes conformed to ~0.5 μm, accompanied by a slight increase in melt pocket aspect ratios (Figure 6).

There may be a stress dependence in the alignment of the melt preferred orientation with respect to the sample-scale stress field. Samples deformed to higher stresses displayed a rotation of the MPO synthetic with the sense of shear away from the loading direction, which is assumed to correspond to σ_1. This rotation might reflect a local deflection of the σ_1 orientation at the piston-sample interface. At relatively higher stresses, the effective direction of σ_1 rotates up to 20˚ synthetically to the sense of shear, as has been observed in quartz and feldspar shear deformation experiments via the development of twinning (Pec & Al Nasser, 2021). As such, the rotation of the grain-scale melt pocket orientation in higher-stress tests is likely a readjustment to the local effective stress field, so that the MPO still remains parallel to the direction of local maximum principal stress.

Examination of some of the samples used in this study with lower resolution optical images (tests PI-277, PI-281, PI-274, and PI-273, as reported in Zimmerman et al., 1999), led to the conclusion that the MPO is inclined at ~20˚ to the shear plane, antithetic to the shear direction (i.e., at ~25˚ to the loading direction). Likewise, analyses of low-resolution optical images of samples deformed in coaxial compression indicated that the MPO also formed at an angle of ~20˚ to the loading direction (Daines & Kohlstedt, 1997; Kohlstedt & Zimmerman, 1996; Zimmerman et al., 1999). Furthermore, melt-rich "bands" observed in experiments on samples with a short compaction length commonly form at an inclination of 15˚ – 20˚ with respect to the shear plane (also reported as 25 – 30˚ from the direction of maximum principal stress) (Holtzman et al., 2003; King et al., 2010; Kohlstedt & Holtzman, 2009). In contrast, our high-resolution data suggests that the grain-scale melt pockets in these samples are aligned parallel to the maximum principal stress. The MPO alignment in our tests is in agreement with observations from analog materials (Takei, 2005) and is consistent with the MPO needed to

produce melt rich "bands" inclined 15 – 20˚ to the shear plane on sample scale within the framework of two-phase flow theory with viscous anisotropy (Katz & Takei, 2013; Takei & Holtzman, 2009c, 2009b, 2009a; Takei & Katz, 2013; Taylor-West & Katz, 2015). Local variations in melt network orientation do exist, as seen in Figure 6; the orientation of larger melt pockets, perhaps as an aggregation of several smaller pockets, can produce local sub-maxima in orientation close to 20˚ for higher-strain samples in which incipient melt segregation is observed.

It appears that the scale of observation and the method of analysis (projection-based methods and autocorrelation-based methods vs. ellipse-fitting methods) may influence estimates of melt orientation. We propose that individual melt pockets at the grain scale align subparallel to σ_1, while aggregate melt pockets on the sample scale form an en echelon pattern aligned at a lower observed angle with respect to σ_1 (Figure 6).

However, this sample-scale alignment at ~20˚ with respect to σ_1 only occurred in our highest-strain sample; sample-scale alignment developed parallel to the direction of σ_1 in all other samples. Melt in the highest strain sample also began to segregate into melt-rich and melt-poor domains, as is typically observed in sheared samples with a short compaction length at strains of $\gamma \geq 1$ (King et al., 2010; Kohlstedt & Holtzman, 2009). The emergence of these "bands" may be the result of viscous anisotropy induced by grain-scale alignment of melt parallel to σ_1 (45˚ to the shear plane) and decreasing compaction length as grains recrystallize to a smaller grain size, documented in Figure 7c. These observations again agree with predictions from the viscous anisotropy theory framework (Katz & Takei, 2013; Quintanilla-Terminel et al., 2019; Takei & Holtzman, 2009c; Taylor-West & Katz, 2015), and explain the discrepancy between experimentally obtained value of 25˚ for melt orientation and computationally predicted sub-parallel orientation with respect to σ_1; both are correct, just at different observation scales. The closer the sample size or observation scale is to the compaction length, the more likely melt is to be oriented at 20˚ to the shear plane; smaller scale melt networks are oriented parallel to σ_1.

4.2 Grain SPO and CPO formation

SPO and CPO form much more slowly than MPO. Grains in the starting material had a SPO and a CPO that developed during hot pressing of the starting material. Individual olivine grains tend to be elongated along the [100] and [001] axes with the longest straight grain boundaries lying in the [010] plane (Miyazaki et al., 2013; Qi et al., 2018). Axial compression of

these elongated crystals aligns the long axes of the SPO in a girdle perpendicular to the loading direction. This process produces a SPO-induced CPO, characterized by girdles in [100] and [001] axes oriented perpendicular to the loading direction and clusters in poles of [010] planes parallel to the loading direction, as seen in Figure 8. At low strains ($0.3 < \gamma < 0.8$), almost no change occurred in the size, orientation, and shape fabric of the grains. The SPO began to define a weak foliation sub-perpendicular to the loading direction at higher strains ($\gamma > 0.8$). The strength of CPO alignment steadily increased with increasing strain in our experiments, consistent with numerical models (Boneh et al., 2015) and other experimental results (Boneh & Skemer, 2014; Hansen et al., 2014; Qi et al., 2018). Although the alignment strength increased, the evolution of grain size and shape fabric still did not depend systematically on strain or stress at low strains. The pole figure geometry also did not change significantly until a strain of $\gamma > 2$.

The CPO of these deformed samples, in which the [010] planes align parallel with the shear direction and the [100] and [001] axis form girdles parallel to the shearing direction, is one commonly observed in sheared aggregates of melt-bearing olivine. This CPO may develop if grains preferentially grow along the [001] direction and then align under the imposed kinematic boundary conditions; the relative fabric strength thus reflects competition between SPO-induced and dislocation-induced CPOs (Qi et al., 2018). Misorientation axes (Figure 10) are also dominantly aligned with [001] with a subordinate maxima around the [010] crystallographic direction, indicating that (010)[100] is the dominant slip system in our rocks, provided that the subgrain walls have a tilt character (Prior et al., 2002) as commonly observed in partially molten olivine rocks (Qi et al., 2018).

The observed CPOs could form by passive rotation of grains with a SPO, or by rotation of individual crystallographic planes due to dislocation motion during deformation. Intracrystalline misorientation maps displayed in Figure 9 confirm that indeed crystalline grains are strongly bent. Geometry of pole figure patterns especially in highest strain samples are similar to an A-type fabric indicative of the easy slip system (010)[100] accommodating deformation in the shear plane (Karato et al., 2008; Zhang & Karato, 1995). The CPO-generating mechanisms (SPO-induced CPO and dislocation-induced CPO) are likely competing at low strains; at higher strains, the more prominent cluster in [100] axes alignment in the shear direction, together with large intragranular misorientations, indicate that dislocation glide is dominant in formation of the CPO.

473 It is interesting to note that in the highest-strain experiments, a secondary cluster in [100]
474 axes orientations forms. This secondary maximum is relatively common in A-type fabrics, but
475 not well understood. Although Zhang et al. (2000) explained this secondary maximum as a
476 signature of non-recrystallized grains in a matrix otherwise undergoing dynamic
477 recrystallization, the grains with this orientation in our sample do not have substantially different
478 misorientations from the bulk sample. They do, however, have a flatter and weaker SPO than all
479 other grains in the sample. More work is necessary to understand the processes governing the
480 formation of this secondary maximum.
481
482 *4.3 Contributions to seismic anisotropy*
483 Measurements of seismic anisotropy in the Earth's lower lithosphere are traditionally
484 understood to result from a CPO, such that seismologists can use the anisotropy measurements to
485 infer the direction of flow in the mantle (Long & Becker, 2010). Any change to the CPO in a
486 given region complicates the interpretation of seismic anisotropy. The presence of melt
487 introduces further difficulties, as MPO will affect the CPO-induced anisotropy. To robustly
488 interpret seismic data, it is important to understand relationships between the kinematic boundary
489 conditions and physical mechanisms involved in creating CPO and MPO in partially molten
490 rocks.
491 Here, we documented that the CPO alignment strengthens, but does not change much in
492 orientation in samples sheared to strains of $\gamma \lesssim 2.5$. In contrast, the grain-scale melt network
493 develops a strong preferred orientation parallel to σ_1 at the onset of deformation, and this
494 orientation persists with increasing strain. The strength of the melt alignment saturates at low
495 strains and does not increase with increasing strain or stress, as can be observed in Figure 5.
496 It follows that at the onset of deformation, the effect of the melt network orientation on
497 seismic anisotropy is pronounced. The presence of aligned melt alone reduced seismic
498 wavespeeds and influenced seismic anisotropies, but the relative alignments of the MPO and
499 CPO determined the extent and magnitude of this change. Because waves are fastest in olivine
500 along the [100] axes and fastest in partially molten material parallel to the direction of the
501 alignment of melt, seismic anisotropy is highest when the [100] axes and the MPO are in a
502 similar orientation. Seismic velocities and anisotropies both decrease at the onset of MPO
503 formation, if the fast crystalline [100] axes are oriented obliquely to the melt preferred

orientation. However, seismic anisotropy increases above $\gamma \approx 0.8$, because the CPO strengthens and the MPO remains unchanged as we demonstrate in Figures 10 and 11.

Previous studies of seismic anisotropy caused by an aligned melt network in a rock with an isotropic CPO determined the strength of anisotropy caused purely by melt orientation (Lee et al., 2017). In a series of tests with the GassDEM model that covered a range of hypothetical MPOs and crystalline fabrics, we found that the interplay of MPO and CPO is crucial to modeling actual seismic anisotropies. As the MPO and the [100] axes of the CPO approach alignment with increasing strain, anisotropy increases; if these two orientations are not aligned, as is the case in the initial stages of deformation, the anisotropy decreases relative to that of the undeformed material. The magnitude of this effect depends on melt fraction as well, such that the effect of co-aligned MPOs and CPOs increases with increasing melt fraction, while the decrease in anisotropy due to competing MPO and CPO did not depend significantly on melt fraction. Anisotropies in Vp wavespeeds, relative travel times of Vs waves, and Vs_1 wavespeeds all followed the trend described here, but the Vs_1 anisotropy is particularly sensitive to the effect of melt fraction. The addition of isotropic (equiaxial) melt reduces seismic velocities and CPO-induced anisotropies but does not interact with the CPO, and so its effect is less pronounced than that of oriented melt.

Our results demonstrate that CPOs and MPOs evolve over distinct characteristic time-scales, complicating the interpretation of observed seismic anisotropy in terms of oriented mantle flow. This conclusion agrees well with studies of fast-deforming zones in Eastern Africa which suggest that melt alignment contributes noticeably to seismic anisotropy in the shallow upper mantle (Bastow et al., 2010; Chambers et al., 2021; Hammond, 2014; Kendall et al., 2005). At greater depths in the mantle where high pressure inhibits partial melting, the CPO is the dominant mechanism for decoding seismic anisotropy and understanding the direction of mantle flow.

The almost instantaneous development of MPO under differential stress also means that MPO is a more reliable indicator of instantaneous changes in stress than the CPO is. An abrupt shift to the local stress field, such as that caused by an earthquake or volcanic eruption, may be visible in seismic signals as a nearly immediate change in the local seismic anisotropy, as MPOs forming due to changing stress will compete with established, steady-state CPOs. This behavior

may be useful for observing results of changes within the Earth, or for understanding melt distribution in rapidly evolving planetary settings dominated by orbital tidal stresses.

5. Conclusions

We found that as a partially molten olivine-basalt aggregate deforms:

- Grain-scale melt alignment forms parallel to σ_1 at the onset of deformation ($0 > \gamma < 0.3$) and persists to the highest strains studied here. Strain does not affect the orientation or strength of this grain-scale melt alignment.
- A distinct sample-scale melt preferred orientation forms 20˚ oblique to σ_1 at higher strain due to en echelon arrangement of grain-scale melt pockets and incipient melt segregation.
- Samples develop a CPO during hot pressing and the pole figure geometry doesn't change significantly over all explored conditions. The strength of the alignment increases steadily with increasing strain.
- SPOs produced during hot-pressing randomize at low to intermediate strains $0.3 > \gamma < 1.3$ and eventually develop a moderately strong SPO oriented at ~30˚ to the shear plane at high strain ($\gamma > 1.3$).
- Melt preferred orientation is established more quickly in response to changes in the stress field than crystallographic preferred orientation or grain shape preferred orientation. The MPO is thus more reactive to changing stress conditions than the CPO.
- As deformation progresses and strain increases, the grain-scale MPO does not change, but the sample-scale melt network coalesces into bands with a secondary orientation. At these higher strains, a dislocation-induced CPO forms and strengthens and hence CPO contributes more to seismic anisotropy than MPO does at high strains.
- At small strains or over short observable timescales, the MPO may thus be more visible than the CPO in changes to seismic anisotropy, providing insight into the stress field orientation in quickly deforming regions of the Earth's upper mantle in ways that CPO-driven anisotropy cannot.

Acknowledgments:

We thank Benjamin Holtzman for commentary and discussion in earlier stages of this project, Rüdiger Kilian for support with MTEX, and Fabrice Barou for providing EBSD maps. David Mainprice for connecting us with Eunyoung Kim who provided support with GassDEM. This work was supported by NSF-EAR 1753482 and NASA-SSW-80NSSC20K0465, with laboratory technician support funded by NSF-EAR 2054414. C.S. also received support from the MIT MathWorks Science Fellowship.

Data availability:

Melt maps, EBSD, and analyzed bulk MPO/SPO data are available at 10.5281/zenodo.7647271.

References:

Almqvist, B. S. G., & Mainprice, D. (2017). Seismic properties and anisotropy of the continental crust: Predictions based on mineral texture and rock microstructure. *Reviews of Geophysics*, *55*(2), 367–433. https://doi.org/10.1002/2016RG000552

Bastow, I. D., Pilidou, S., Kendall, J.-M., & Stuart, G. W. (2010). Melt-induced seismic anisotropy and magma assisted rifting in Ethiopia: Evidence from surface waves. *Geochemistry, Geophysics, Geosystems*, *11*(6). https://doi.org/10.1029/2010GC003036

Blackman, D. K., & Kendall, J.-M. (1997). Sensitivity of teleseismic body waves to mineral texture and melt in the mantle beneath a mid–ocean ridge. *Philosophical Transactions of the Royal Society of London. Series A: Mathematical, Physical and Engineering Sciences*, *355*(1723), 217–231.

Boneh, Y., Morales, L. F. G., Kaminski, E., & Skemer, P. (2015). Modeling olivine CPO evolution with complex deformation histories: Implications for the interpretation of seismic anisotropy in the mantle. *Geochemistry, Geophysics, Geosystems*, *16*(10), 3436–3455. https://doi.org/10.1002/2015GC005964

593 Boneh, Y., & Skemer, P. (2014). The effect of deformation history on the evolution of olivine CPO. *Earth*
594 *and Planetary Science Letters*, *406*, 213–222. https://doi.org/10.1016/j.epsl.2014.09.018
595 Chambers, E. L., Harmon, N., Rychert, C. A., & Keir, D. (2021). Variations in melt emplacement beneath
596 the northern East African Rift from radial anisotropy. *Earth and Planetary Science Letters*, *573*,
597 117150. https://doi.org/10.1016/j.epsl.2021.117150
598 Daines, M. J., & Kohlstedt, D. L. (1997). Influence of deformation on melt topology in peridotites. *Journal*
599 *of Geophysical Research: Solid Earth*, *102*(B5), 10257–10271.
600 https://doi.org/10.1029/97JB00393
601 Hammond, J. O. S. (2014). Constraining melt geometries beneath the Afar Depression, Ethiopia from
602 teleseismic receiver functions: The anisotropic H-κ stacking technique. *Geochemistry,*
603 *Geophysics, Geosystems*, *15*(4), 1316–1332. https://doi.org/10.1002/2013GC005186
604 Hansen, L. N., Faccenda, M., & Warren, J. M. (2021). A review of mechanisms generating seismic
605 anisotropy in the upper mantle. *Physics of the Earth and Planetary Interiors*, *313*, 106662.
606 https://doi.org/10.1016/j.pepi.2021.106662
607 Hansen, L. N., Zhao, Y.-H., Zimmerman, M. E., & Kohlstedt, D. L. (2014). Protracted fabric evolution in
608 olivine: Implications for the relationship among strain, crystallographic fabric, and seismic
609 anisotropy. *Earth and Planetary Science Letters*, *387*, 157–168.
610 https://doi.org/10.1016/j.epsl.2013.11.009
611 Heilbronner, R., & Barrett, S. (2014). *Image Analysis in Earth Sciences: Microstructures and Textures of*
612 *Earth Materials*. Springer-Verlag. https://doi.org/10.1007/978-3-642-10343-8
613 Hier-Majumder, S. (2011). Development of anisotropic mobility during two-phase flow. *Geophysical*
614 *Journal International*, *186*(1), 59–68. https://doi.org/10.1111/j.1365-246X.2011.05024.x

615 Holtzman, B. K., Groebner, N. J., Zimmerman, M. E., Ginsberg, S. B., & Kohlstedt, D. L. (2003). Stress-
616 driven melt segregation in partially molten rocks. *Geochemistry, Geophysics, Geosystems*, *4*(5).
617 https://doi.org/10.1029/2001GC000258
618 Holtzman, B. K., & Kendall, J.-M. (2010). Organized melt, seismic anisotropy, and plate boundary
619 lubrication. *Geochemistry, Geophysics, Geosystems*, *11*(12).
620 https://doi.org/10.1029/2010GC003296
621 Karato, S., Jung, H., Katayama, I., & Skemer, P. (2008). Geodynamic Significance of Seismic Anisotropy of
622 the Upper Mantle: New Insights from Laboratory Studies. *Annual Review of Earth and Planetary*
623 *Sciences*, *36*(1), 59–95. https://doi.org/10.1146/annurev.earth.36.031207.124120
624 Katz, R. F., & Takei, Y. (2013). Consequences of viscous anisotropy in a deforming, two-phase aggregate.
625 Part 2. Numerical solutions of the full equations. *Journal of Fluid Mechanics*, *734*, 456–485.
626 https://doi.org/10.1017/jfm.2013.483
627 Kendall, J.-M., Stuart, G. W., Ebinger, C. J., Bastow, I. D., & Keir, D. (2005). Magma-assisted rifting in
628 Ethiopia. *Nature*, *433*(7022), Article 7022. https://doi.org/10.1038/nature03161
629 Kim, E., Kim, Y., & Mainprice, D. (2019). GassDem: A MATLAB program for modeling the anisotropic
630 seismic properties of porous medium using differential effective medium theory and
631 Gassmann's poroelastic relationship. *Computers & Geosciences*, *126*, 131–141.
632 https://doi.org/10.1016/j.cageo.2019.02.008
633 King, D. S. H., Zimmerman, M. E., & Kohlstedt, D. L. (2010). Stress-driven Melt Segregation in Partially
634 Molten Olivine-rich Rocks Deformed in Torsion. *Journal of Petrology*, *51*(1–2), 21–42.
635 https://doi.org/10.1093/petrology/egp062
636 Kohlstedt, D. L., & Holtzman, B. K. (2009). Shearing Melt Out of the Earth: An Experimentalist's
637 Perspective on the Influence of Deformation on Melt Extraction. *Annual Review of Earth and*
638 *Planetary Sciences*, *37*(1), 561–593. https://doi.org/10.1146/annurev.earth.031208.100104

639 Kohlstedt, D. L., & Zimmerman, M. E. (1996). Rheology of Partially Molten Mantle Rocks. *Annual Review*
640 *of Earth and Planetary Sciences*, *24*(1), 41–62. https://doi.org/10.1146/annurev.earth.24.1.41
641 Lee, A. L., Walker, A. M., Lloyd, G. E., & Torvela, T. (2017). Modeling the impact of melt on seismic
642 properties during mountain building. *Geochemistry, Geophysics, Geosystems*, *18*(3), 1090–1110.
643 https://doi.org/10.1002/2016GC006705
644 Long, M. D., & Becker, T. W. (2010). Mantle dynamics and seismic anisotropy. *Earth and Planetary*
645 *Science Letters*, *297*(3), 341–354. https://doi.org/10.1016/j.epsl.2010.06.036
646 Mainprice, D. (1997). Modelling the anisotropic seismic properties of partially molten rocks found at
647 mid-ocean ridges. *Tectonophysics*, *279*(1), 161–179. https://doi.org/10.1016/S0040-
648 1951(97)00122-4
649 Miyazaki, T., Sueyoshi, K., & Hiraga, T. (2013). Olivine crystals align during diffusion creep of Earth's
650 upper mantle. *Nature*, *502*(7471), Article 7471. https://doi.org/10.1038/nature12570
651 Paterson, M. S. (1990). Rock Deformation Experimentation. In *The Brittle-Ductile Transition in Rocks* (pp.
652 187–194). American Geophysical Union (AGU). https://doi.org/10.1029/GM056p0187
653 Pec, M., & Al Nasser, S. (2021). Formation of Nanocrystalline and Amorphous Materials Causes Parallel
654 Brittle-Viscous Flow of Crustal Rocks: Experiments on Quartz-Feldspar Aggregates. *Journal of*
655 *Geophysical Research: Solid Earth*, *126*(5), e2020JB021262.
656 https://doi.org/10.1029/2020JB021262
657 Prior, D. J., Wheeler, J., Peruzzo, L., Spiess, R., & Storey, C. (2002). Some garnet microstructures: An
658 illustration of the potential of orientation maps and misorientation analysis in microstructural
659 studies. *Journal of Structural Geology*, *24*(6), 999–1011. https://doi.org/10.1016/S0191-
660 8141(01)00087-6
661 Qi, C., Hansen, L. N., Wallis, D., Holtzman, B. K., & Kohlstedt, D. L. (2018). Crystallographic Preferred
662 Orientation of Olivine in Sheared Partially Molten Rocks: The Source of the "a-c Switch."

Geochemistry, Geophysics, Geosystems, *19*(2), 316–336. https://doi.org/10.1002/2017GC007309

Quintanilla-Terminel, A., Dillman, A. M., Pec, M., Diedrich, G., & Kohlstedt, D. L. (2019). Radial Melt Segregation During Extrusion of Partially Molten Rocks. *Geochemistry, Geophysics, Geosystems*, *20*(6), 2985–2996. https://doi.org/10.1029/2018GC008168

Savage, M. K. (1999). Seismic anisotropy and mantle deformation: What have we learned from shear wave splitting? *Reviews of Geophysics*, *37*(1), 65–106. https://doi.org/10.1029/98RG02075

Takei, Y. (2001). Stress-induced anisotropy of partially molten media inferred from experimental deformation of a simple binary system under acoustic monitoring. *Journal of Geophysical Research: Solid Earth*, *106*(B1), 567–588. https://doi.org/10.1029/2000JB900361

Takei, Y. (2005). Deformation-induced grain boundary wetting and its effects on the acoustic and rheological properties of partially molten rock analogue. *Journal of Geophysical Research: Solid Earth*, *110*(B12). https://doi.org/10.1029/2005JB003801

Takei, Y., & Holtzman, B. K. (2009a). Viscous constitutive relations of solid-liquid composites in terms of grain boundary contiguity: 1. Grain boundary diffusion control model. *Journal of Geophysical Research: Solid Earth*, *114*(B6). https://doi.org/10.1029/2008JB005850

Takei, Y., & Holtzman, B. K. (2009b). Viscous constitutive relations of solid-liquid composites in terms of grain boundary contiguity: 2. Compositional model for small melt fractions. *Journal of Geophysical Research: Solid Earth*, *114*(B6). https://doi.org/10.1029/2008JB005851

Takei, Y., & Holtzman, B. K. (2009c). Viscous constitutive relations of solid-liquid composites in terms of grain boundary contiguity: 3. Causes and consequences of viscous anisotropy. *Journal of Geophysical Research: Solid Earth*, *114*(B6). https://doi.org/10.1029/2008JB005852

685 Takei, Y., & Katz, R. F. (2013). Consequences of viscous anisotropy in a deforming, two-phase aggregate.
686 Part 1. Governing equations and linearized analysis. *Journal of Fluid Mechanics*, *734*, 424–455.
687 https://doi.org/10.1017/jfm.2013.482
688 Taylor-West, J., & Katz, R. F. (2015). Melt-preferred orientation, anisotropic permeability and melt-band
689 formation in a deforming, partially molten aggregate. *Geophysical Journal International*, *203*(2),
690 1253–1262. https://doi.org/10.1093/gji/ggv372
691 Zhang, S., & Karato, S. (1995). Lattice preferred orientation of olivine aggregates deformed in simple
692 shear. *Nature*, *375*(6534), 774–777. https://doi.org/10.1038/375774a0
693 Zhang, S., Karato, S., Fitz Gerald, J., Faul, U. H., & Zhou, Y. (2000). Simple shear deformation of olivine
694 aggregates. *Tectonophysics*, *316*(1–2), 133–152. https://doi.org/10.1016/S0040-1951(99)00229-
695 2
696 Zimmerman, M. E., Zhang, S., Kohlstedt, D. L., & Karato, S. (1999). Melt distribution in mantle rocks
697 deformed in shear. *Geophysical Research Letters*, *26*(10), 1505–1508.
698 https://doi.org/10.1029/1999GL900259
699
700